An Integrated Permanent-Magnet Microturbogenerator Supported on Microball Bearings

Mustafa Ilker Beyaz, *Member, IEEE*, Brendan Michael Hanrahan, *Member, IEEE*, Jeremy Feldman, and Reza Ghodssi, *Member, IEEE*

Abstract—This paper presents the design, fabrication, and testing of an integrated microturbogenerator utilizing permanent magnets and microball bearings. The key components of this generator are the following: 1) a silicon microturbine rotor housing thick magnetic components; 2) encapsulated microball bearings providing a simple actuation scheme and a robust support structure; and 3) wafer-thick stator coils. The microturbogenerator was designed and fabricated to have a ten-pole rotor and a ten-pole three-turns-per-pole stator. The impedance of the stator coils was shown to be a purely resistive 220 Ω up to 10 kHz. The spin-down characterization of the rotor revealed a dynamic friction torque of 33 μN · m at a rotational speed of 16 kilo rotations per minute (krpm), corresponding to 6% turbine efficiency. The maximum per-phase ac open-circuit voltage and power were measured to be 0.1 V and 5.6 μW on a matched load at 23 krpm, respectively, in full agreement with theoretical analysis and performance estimations. The microturbogenerator presented in this paper provides a flexible design platform for further improvement and will lead to the development of next-generation integrated microturbogenerators offering high power, simple operation, and robust mechanics. [2012-0186]

Index Terms—Microball bearings, microgenerator, microturbogenerator, power microelectromechanical systems (MEMS).

I. INTRODUCTION

THE development of small-scale and high-density energy sources is becoming increasingly necessary to improve the capabilities and operation lifetimes of portable electronic systems. Accordingly, the miniaturization of large-scale portable generators running on hydrocarbon fuels down to microelectromechanical systems (MEMS) dimensions has been of particular interest due to the high energy density of these fuels surpassing that of the battery technology. Magnetic electromechanical generators with or without turbine parts are integral components of these power systems driven by combustion engines. Hence, the demonstration of magnetic microscale electromechanical generators (microgenerators) is essential for the development of hydrocarbon-based as well as other gas flow-driven MEMS power sources.

Several studies have been conducted to investigate the effect of downscaling on magnetic generators, reporting the advantages of using permanent magnets over self-excited induction machines [1]–[3]. Accordingly, the research in this field has taken advantage of permanent magnets as magnetic field sources. An axial-flow and axial-flux permanent-magnet microturbogenerator was reported by Holmes *et al.* [3]. The generator was designed to have an SU-8 polymer rotor with NdFeB magnets supported by off-the-shelf ball-race bearings over a silicon stator with spiral Cu windings. An induced peak-to-peak open-circuit voltage of 1.19 V was measured at a rotational speed of 30 kilo rotations per minute (krpm), yielding an ac output power of 1.1 mW on a 40-Ω matched load. Pan and Wu presented an axial-flux permanent-magnet generator measuring 5 mm in diameter with eight NdFeB magnets [4]. An alternative coil fabrication was developed to create a four-layer Cu winding on the stator with a coil resistance of 30 Ω. The rotor was spun using an external spindle at 2.2 krpm and generated a 0.412-mW ac power. The same authors later reported the fabrication of stator coils using low-temperature cofired ceramic materials. With this technique and some modifications in the test setup, an ac output power of 1.89 mW was generated at 13 krpm [5]. Raisigel *et al.* presented a microturbogenerator with turbine structures defined on the permanent-magnet rotor measuring 8 mm in diameter [6]. The stator component utilized a three-phase, planar, overlapped, and multiturn winding design with electroplated coil structures having 2–5-Ω resistance. The rotor was rotated up to 58 krpm on magnetopneumatic bearings, resulting in a 14-mW ac power. To spin the device at higher speeds, the authors used a dental drill, achieved rotational speeds up to 400 krpm, and generated 5 W power over wye-connected 12-Ω resistors.

A three-phase axial-flux permanent-magnet generator with low resistance windings was demonstrated by Arnold *et al.* [7]. By electroplating planar Cu coil windings up to 120 μm, the coil resistance was decreased down to 0.1 Ω. The stator substrate was made of permalloy rather than silicon to increase magnetic flux density. The rotor was composed of SmCo

M. I. Beyaz was with the University of Maryland, College Park, MD 20742, USA. He is now with Antalya International University, Antalya, 07190, Turkey (e-mail: mibeyaz@antalya.edu.tr).

B. M. Hanrahan is with the University of Maryland, College Park, MD 20742 USA, and also with the U.S. Army Research Laboratory, Adelphi, MD 20783 USA (e-mail: bhanrah@gmail.com).

J. Feldman and R. Ghodssi are with the University of Maryland, College Park, MD 20742 USA (e-mail: jfn@umd.edu; ghodssi@umd.edu).

magnets with Hiperco 50 attached on the backside, measuring 9.5 mm in diameter. Actuated by an external spindle, the device generated a 1.1-W dc power on a 25-Ω load at 120 krpm. The same group presented a second-generation device with more efficient coil design and a more robust rotor with a titanium housing, resulting in 12-W ac and 8-W dc powers on 37 Ω at 305 krpm [8]. In parallel, an air bearing-supported turbine rotor with NdFeB permanent magnets was demonstrated by Yen *et al.* and integrated with the stator design presented in [8] with a drop-in winding method to develop an integrated microturbogenerator [9]. The device was able to produce an ac power of 19 mW at 40 krpm. Finally, Herrault *et al.* further miniaturized the device in [8] and fabricated an axial-flux permanent-magnet generator with a diameter of 2 mm [10]. The device was actuated using external testing apparatus and produced 6.6 mW at 392 krpm. The same authors improved the design presented in [8] by adding laminated permalloy structure on the stator and achieved a 1.05-W ac power at 200 krpm [11].

A major aspect for the development of a fully integrated microturbogenerator, and fast-rotating micromachines in general, is the design and incorporation of a MEMS bearing mechanism that can enable the following: 1) simple device operation with no need for external actuation components and 2) robust mechanical structure for device reliability. These qualities are specifically necessary when the device is integrated with a future microcombustion engine and taken out of laboratory environment to generate power in the field. Microball bearings are envisioned to be a viable support mechanism in this direction and have been rigorously studied by our group [12]–[19]. Ghalichechian *et al.* demonstrated a linear micromotor supported on microball bearings with a variable capacitance actuation mechanism and achieved speeds on the order of 7 mm/s [12]. The improvement of the speed and positioning accuracy was later demonstrated through the implementation of a closed-loop control system in [13]. A rotary version of this device was also presented with a rotational speed and net produced torque of 517 rpm and 5.62 μN · m, respectively [14]. In parallel, Waits *et al.* pioneered the development of the encapsulated microball bearing technology [15] and utilized it to fabricate a micropump for fluid delivery in the small scale [16]. Rotational speeds and pumping rates up to 87 krpm and 80 mL/h, respectively, were achieved with pneumatic actuation. Detailed friction and wear characterization of encapsulated microball bearings was performed by McCarthy *et al.* [17]. The dependence of friction on rotational speed and normal force was thoroughly investigated and reported. Finally, a rotary electrostatic microactuator was presented by McCarthy *et al.* in [18] with repeatable operation up to 2 krpm. These studies and investigations have demonstrated the robustness, stability, low friction, and low wear characteristics of microball bearings that are desired for fast-rotating MEMS devices. In addition, it was shown that the microball bearings do not require external magnetic, mechanical, or pneumatic apparatus for actuation.

Building upon our previous studies on microball bearings, this paper presents the development of an integrated microturbogenerator capable of converting gas flow into electricity. In addition to microball bearings providing a simple actuation and robust mechanics, the key components of this platform include
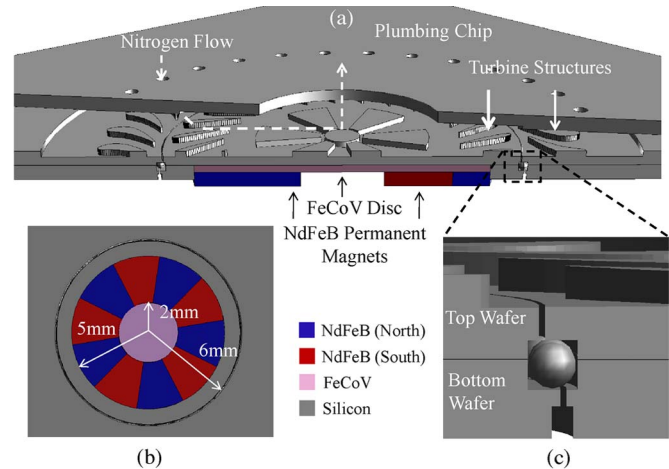

Fig. 1. Three-dimensional schematic views of the rotor showing (a) general structure and actuation, (b) permanent magnets on the bottom, and (c) encapsulated microball bearings.

a microturbine rotor with thick magnetic structures and wafer-thick stator coils. While thick magnetics in the rotor provide high magnetic flux density, the thickness of the stator optimizes the flux linkage to the coils. Fabricating 80% of the total coil length within the stator wafer is also an important step for further decreasing the coil resistance in future implementations. We previously reported the development of individual components as well as their integration in latest conferences [19]–[21]. This paper expands upon our previous work and reports detailed theoretical analysis, simulation results, a comprehensive and extended characterization, and several aspects of this work prone to further improvement.

II. DESIGN

The integrated microturbogenerator presented in this paper is composed of a turbine rotor with permanent magnets and a high-magnetic-permeability disk (back iron), a stator with three-phase planar copper coils, and encapsulated microball bearings incorporated into the rotor. The device utilizes Faraday's law of electromagnetic induction to convert the pneumatic actuation of the rotor, and hence the mechanical energy, into electricity. The following sections describe the design details and present theoretical analysis and simulations.

A. Rotor With Integrated Microball Bearings

While the fundamental rotor design is based on the silicon microturbines presented in [15]–[18], a number of structural changes were implemented to facilitate the integration of magnetic materials. The rotor, shown in Fig. 1(a)–(c), is composed of two 500-μm-thick silicon wafers bonded together, encapsulating microballs ($\varnothing = 285$ μm) in between pre-etched trenches. The top rotor wafer has radial in-flow turbine structures etched 200 μm deep in silicon for pneumatic actuation. A separate silicon plumbing chip with etched through holes is placed on top of the rotor, guiding the compressed nitrogen flow to spin the rotor [see Fig. 1(a)]. An etched cavity is defined on the bottom rotor wafer to accommodate permanent magnets and a back iron disk.
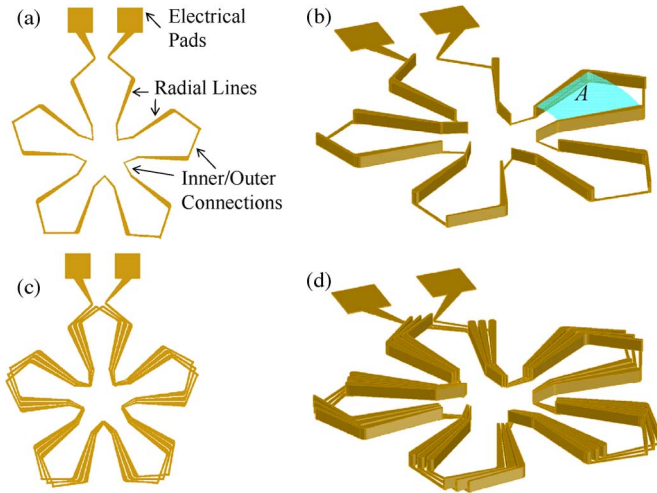
Fig. 2.   One-phase coil configuration showing (a and b) ten-pole one-turn-per-pole design connection scheme and angled view and (c and d) ten-pole three-turns-per-pole design connection scheme and angled view.

NdFeB is selected as the permanent-magnet material mainly due to its high remanent flux density of up to 1.4 T. Fig. 1(b) illustrates a schematic of the bottom side of the rotor showing the ten discrete, off-the-shelf, premagnetized, and pie-shaped magnets (N52, Magnet Applications) arranged in alternating magnetic polarity. The inner and outer radii of the magnets were selected to be 2 and 5 mm, respectively, to increase the device area and magnetic flux as much as possible while remaining within the fabrication limitations due to yield considerations. To provide a robust housing for the magnets, the rotor radius was selected to be 6 mm, which is a 1-mm increase in comparison to the previous demonstrations of the microturbines in [15]–[18]. The minimum thickness of the permanent magnets was bound to commercial availability and set to be 500 μm.

The role of high-permeability back iron is to enhance the magnetic flux density within the stator by decreasing the magnetic reluctance of the flux pathway. The back iron material is determined to be FeCoV (Goodfellow Corporation) due to its high magnetic permeability ($\mu_r \sim 3000$) and high saturation flux density of 2.4 T. The thickness of this component should be carefully selected to minimize the magnetic saturation. While the effect of a low-thickness (< 50 μm) FeCoV may be negligible for the given magnet area and volume, thicknesses larger than 500 μm are difficult to integrate within a MEMS frame. Accordingly, the thickness of this component was set to be 250 μm which ensures that the half thickness of the magnets will be enclosed by the rotor. The simulations also showed that the 250-μm thickness of FeCoV will prevent magnetic saturation and hence increase the flux density through the stator. A close-up view of the stainless steel microball bearings is also presented in Fig. 1(c) that shows the central rotor released from the outer stationary frame.

B. Stator

The stator is composed of three-phase planar copper coils embedded in a silicon substrate. A planar overlapping coil structure is preferred to use the active stator area more ef-

fectively. The basic one-phase ten-pole one-turn coil design shown in Fig. 2(a) and (b) is a combination of radial lines and inner/outer connections. Five loops in one turn with active area A, matching that of the magnets, ensure the simultaneous alignment of five north or south poles. While only the radial parts of the coils contribute to voltage induction, the inner/outer connections are used to serially connect them for additive voltage generation. Fig. 2(c) and (d) shows the one-phase ten-pole three-turns-per-pole coil design that is constructed by serially connecting three separate one-turn designs slightly shifted in space relative to each other to further amplify the voltage. A three-phase design is structured by arranging three of these phases around the stator with $2\pi/3$ electrical radians with respect to each other. Unlike coils at larger length scales, the resistance is the dominant impedance factor over inductance in MEMS-scale coils [6]–[11].

While the overall coil structure and connection scheme is similar to that of the devices in [6]–[11], the stator design described here differs due to the high thicknesses involved in the coil structure. The radial parts of the coils are designed to have a thickness of 400 μm for two reasons: 1) The future implementations of this device will have a separate back iron beneath the stator coils for even higher magnetic flux density within the stator, and in this case, 400-μm-thick coils are shown to yield the optimum magnetic linkage and low resistance as described in the following sections; and 2) compared to the geometry, thickness, and resultant electrical parameters of the coils in [6]–[11], the demonstration of this design is an important step forward to achieve coil resistances of less than 0.1 Ω for higher levels of power generation. Due to the high coil thickness, the stator is made of a silicon wafer as a coil housing structure. The radial parts of the coils as well as half of the inner and outer connections, which corresponds to approximately 80% of the complete coil length, are embedded in the stator wafer by electroplating technique as shown in Fig. 3(a)–(c). The three-phase overlapping coil design mandates a 3-D connection scheme. Accordingly, the remainder of the connections is formed on the bottom side of the stator over a patterned dielectric material [see Fig. 3(b)]. The thickness of this part of the coils is selected to be three orders of magnitude lower than that of the radial lines to decrease the fabrication complexity and demonstrate the first functional device.

C. Theory and Optimization

The device operation is based on Faraday's law of electromagnetic induction as described by

$$V_{\text{coil}} = \frac{d}{dt} \int B(t) \times dA \qquad (1)$$

where V_{coil} is the open-circuit voltage induced between the terminals of the radial coil loop with area A in Fig. 2(b) due to the time-varying magnetic flux density $B(t)$. Equation (1) can be rewritten as

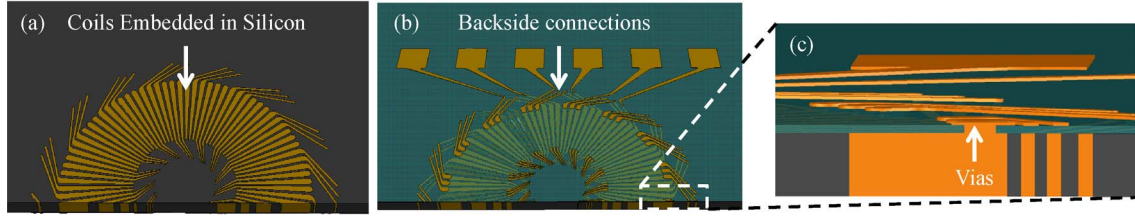$$V_{\text{coil}} = A \times \frac{dB(t)}{dt}. \qquad (2)$$

Fig. 3. Three-dimensional cutaway schematics of the stator showing (a) 80% of the copper coils embedded in silicon, (b) backside connections over a dielectric layer, and (c) vias and connections.

Although $B(t)$ is a sinusoidal-like function due to the leakage fluxes and imperfect magnetization profile of permanent magnets, it can be approximated as a triangular waveform $B_{\text{avg}}(t)$ oscillating between $\pm B_{\text{avg}}$ to carry on the analysis, where B_{avg} is the magnitude of the flux density on A at perfect magnet–coil alignment. When the rotor is rotating at a speed of ω in rpm, the mechanical frequency of the system becomes $\omega/60$. Since the electrical frequency of the system is $(P/2) \times (\omega/60)$, the transition time from $+B_{\text{avg}}$ to $-B_{\text{avg}}$ becomes $60/P\omega$, where P is the number of poles. Therefore, (2) becomes

$$V_{\text{coil}} = \frac{2 \times A \times B_{\text{avg}} \times P \times \omega}{60}. \tag{3}$$

Since $A = (\pi \times (r_{\text{out}}^2 - r_{\text{in}}^2))/P$, with r_{out} and r_{in} being the outer and inner radii of the radial part of the coils, respectively, (3) can be rewritten as

$$V_{\text{coil}} = \frac{2 \times B_{\text{avg}} \times \pi \times \left(r_{\text{out}}^2 - r_{\text{in}}^2\right) \times \omega}{60}. \tag{4}$$

There are $P/2$ radial coil loops in one turn as shown in Fig. 2(a). Therefore, for an N-turns-per-pole device, the single-phase open-circuit V_{OC} becomes

$$V_{\text{OC}} = \frac{P \times N \times B_{\text{avg}} \times \pi \times \left(r_{\text{out}}^2 - r_{\text{in}}^2\right) \times \omega}{60}. \tag{5}$$

The $P \times N$ product represents the number of radial lines that are present in the coil structure and should be maximized for a higher induced voltage. Since microscale coils can be considered as purely resistive at the frequency range of interest [6]–[11], the maximum output power P_{OUT} in the matched electrical load condition can be described by the proportionality

$$P_{\text{OUT}} \propto \frac{V_{\text{OC}}^2}{R_{\text{phase}}} \tag{6}$$

where R_{phase} is the phase resistance consisting of $(P \times N)/2$ radial loops [see Fig. 2(b)]. A study by Das et al. showed that, in similar planar overlapping coil structures, $R_{\text{phase}} \propto ((P \times N)^2/t_{\text{coil}})$, where t_{coil} is the thickness of the radial parts of the coils [22]. When this is combined with (5) and (6), we obtain

$$P_{\text{OUT}} \propto B_{\text{avg}}^2 \times t_{\text{coil}} \times \left[\pi \times \left(r_{\text{out}}^2 - r_{\text{in}}^2\right)\right]^2 \times \omega^2. \tag{7}$$

It is clear from (7) that the active area defined by r_{out} and r_{in} have a substantial effect on power. While increasing r_{out} would tremendously improve the output power, fabricating large-area structures in MEMS poses significant challenges. Similarly, a
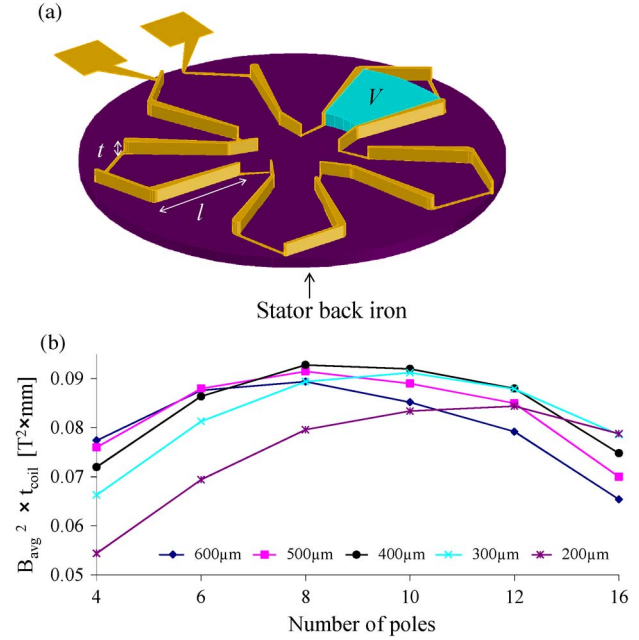

Fig. 4. (a) Domain V considered in the simulations and the stator back iron included in the analysis. $t = 400 \ \mu m$, and $l = r_{\text{out}} - r_{\text{in}} = 3$ mm. (b) Value of $B_{\text{avg}}^2 \times t_{\text{coil}}$ for varying number of poles and coil thicknesses.

low r_{in} value increases the output power and fabrication complexity, simultaneously, due to the area required for the inner connection scheme [see Fig. 3(b)]. Considering these factors, r_{out} and r_{in} were selected to be 5 and 2 mm, respectively. The only other design parameters in (7) are the coil thickness and average flux magnetic density, which are determined by the device geometry and number of permanent magnets.

To improve the $B_{\text{avg}}^2 \times t_{\text{coil}}$ product, a separate FeCoV back iron attached at the bottom of the stator is envisioned in future implementations that would decrease the magnetic reluctance of the stator and increase B_{avg}. In the presence of a stator back iron component [see Fig. 4(a)], higher coil thicknesses increase t_{coil} while decreasing B_{avg} due to the increased distance between the rotor magnets and the stator back iron. In addition to these two competing effects, the number of poles should be carefully selected to find the optimum balance between the magnetic field leakage and magnetic saturation taking effect inside the rotor back iron. Accordingly, the $B_{\text{avg}}^2 \times t_{\text{coil}}$ product was investigated for a number of magnetic poles and varying coil thicknesses using a finite-element simulation software (COMSOL). The average magnetic flux density squared was found by computing the integral $B_{\text{avg}}^2 = (1/V)\int_V B^2 dV$, where V corresponds to the volume of one radial coil loop
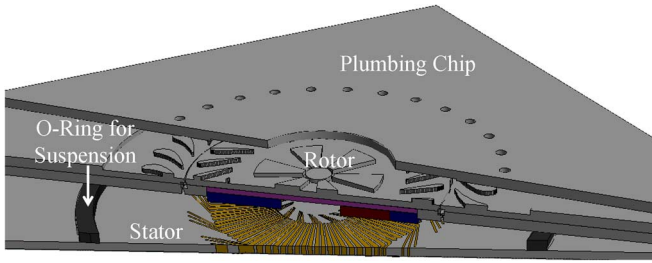
Fig. 5.   Three-dimensional schematic of the microturbogenerator.

[see Fig. 4(a)]. Simulation results are presented in Fig. 4(b). The air gap between the magnets and stator surface was set to be 50 μm, which provides enough tolerance for fabrication and assembly imperfections.

The simulation results show that, for a given thickness, the average magnetic flux density decreases at the following: 1) decreasing number of poles due to magnetic saturation in the rotor back iron and 2) increasing number of poles due to magnetic flux leakage between adjacent poles. The highest value of the $B_{\mathrm{avg}}^2 \times t_{\mathrm{coil}}$ product was obtained at the coil thickness of 400 μm. Accordingly, three designs with 8, 10, and 12 poles yielding the highest values at this thickness were selected to pursue fabrication. The numbers of turns for these three different designs were selected to be 4, 3, and 3, respectively, to increase the number of radial coils as much as possible while keeping the aspect ratio of radial lines on the order of 20 to avoid the fabrication challenges.

Although included in the simulations, some design aspects were modified to decrease the fabrication and operation complexity and to demonstrate the first functional device. First, the magnetic field simulations showed that the magnetic force between the stator back iron and permanent magnets is as high as 5 N. As this may result in excessive wear in the ball raceway shown in Fig. 1(c), the stator back iron beneath the coils was excluded. In addition, although the rotor–stator gap was initially designed to be 50 μm through microfabrication, an O-ring was used instead to suspend the rotor over the stator as well as to seal the rotor backside for lower fabrication complexity, leading to wider gaps between these two components. These aspects are left as future improvements to be implemented for higher performance. The schematic of a complete microturbogenerator is shown in Fig. 5.

III. FABRICATION

A. Rotor With Integrated Microball Bearings

The fabrication of the microturbogenerator involved many processing challenges due to the number of components and active layers combined together. Initially, 3-μm-thick oxide layers were patterned on both sides of the 500-μm-thick top and bottom rotor wafers as deep reactive ion etching (DRIE) masks [see Fig. 6(a)]. Next, two-step DRIE processes using the oxide layer and an additional photoresist etch mask were performed on the sides of both wafers facing each other to create 145-μm-deep ball alignment pits and ball raceways with depths of 95 μm on the top wafer and 195 μm on the bottom wafer [15]–[17] [see Fig. 6(b)]. Release areas on both wafers
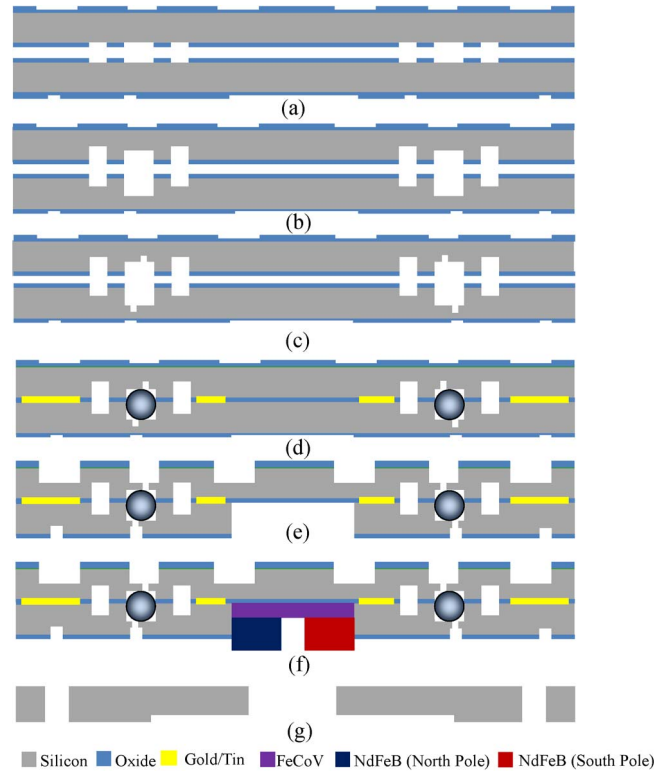

Fig. 6.   Fabrication of the rotor: (a)–(c) Definition of microball raceways, (d) ball encapsulation, (e) and (f) rotor release and magnetic material integration, and (g) plumbing chip.

were defined by lithography with spray-coated photoresist and a subsequent DRIE step at the bottom of the raceway [see Fig. 6(c)]. A ring-shaped eutectic bonding layer that consists of a stack of 50-nm Cr, 50-nm Au, 1-μm AuSn (74/26), and 50-nm Au metals was evaporated through a shadow mask over the rotor wafers. The 5.15/5.65 mm inner/outer radii of this layer surround the periphery of the magnetic housing defined in the subsequent steps. The raceway on the bottom wafer was filled with ~100 microballs ($\varnothing = 285$ μm), covering roughly 75% of the raceway and ensuring that the rotor will not collapse on one side in case all the microballs are bunched together. Using the ball alignment technique developed by Waits et al. in [15] and [16], the two wafers were aligned and bonded at 330 °C with a 3000-N force in H_2N_2 gas at atmospheric pressure [see Fig. 6(d)]. Next, a 300-μm-deep DRIE was performed on the bottom side as an initial step to define the magnetic housing. Finally, 200-μm-deep timed DRIE steps were applied on the top and bottom sides of the rotor assembly to release the rotor from the peripheral frame and define the 500-μm-deep magnetic housing along with 200-μm-high turbine blades [see Fig. 6(e)]. The radius of the magnetic housing was selected to be 5.1 mm, which is slightly larger than the 5-mm magnet radius to provide enough tolerance for integration. Permanent magnets were assembled on the FeCoV disk separately and then bonded to the rotor using epoxy [see Fig. 6(f)]. In parallel, the plumbing chip was fabricated using two DRIE steps performed on the both sides of the wafer to define through holes for gas flow as well as a 50-μm cavity above turbine blades [see Fig. 6(g)].

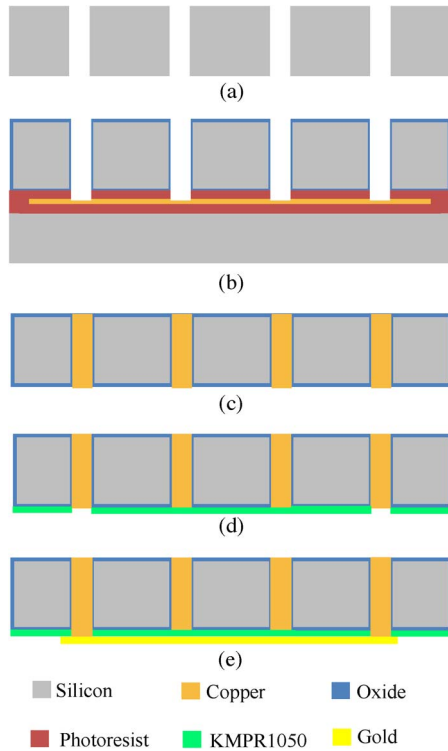| Silicon | | Copper | | Oxide |
| Photoresist | | KMPR1050 | | Gold |

Fig. 7. Stator fabrication showing (a) definition of coil pattern in silicon, (b) bottom–up electroplating technique with photoresist-based separation method, (c) electroplating of the coil pattern, (d) KMPR1050 patterning for via formation, and (d) Au patterning to create backside connections.
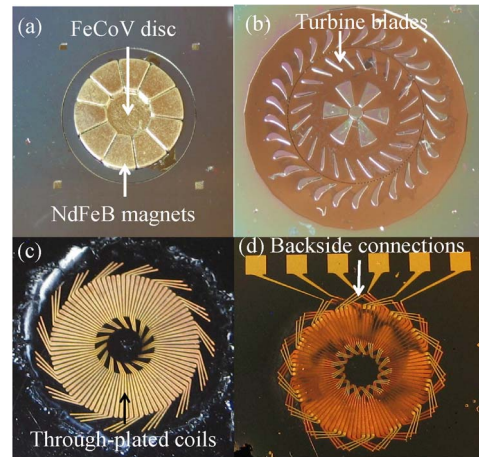

Fig. 8. Photographs of the (a) bottom side of the rotor, (b) top side of the rotor, (c) top side of the stator, and (d) backside of the stator.

Possible improvements for this process are explained in the Discussion section. Pictures of a fabricated ten-pole rotor and a ten-pole three-turns-per-pole stator are shown in Fig. 8.

IV. TESTING AND RESULTS

A. Experimental Apparatus

A schematic view and a picture of the packaged device are shown in Figs. 9 and 10, respectively. The microturbogenerator is packaged between two plastic manifolds providing a 100-μm stator–rotor alignment tolerance with compliant O-rings. The testing orientation was determined to be upside-down for a simple electrical connection scheme. Compressed nitrogen is provided through the plastic manifold while an optical displacement sensor located at the central exit of the packaging tracks the rotation of the etched structures on the rotor for speed measurements. A LabVIEW program was used for real-time monitoring of turbine pressure, gas flow rate, rotor speed, and generated voltage. The nitrogen flow induces a net pressure higher than ambient in the sealed volume between the rotor and the stator, pushing the rotor down and ensuring rotation on the planar raceway surface [15]–[18]. Prior to testing the microturbogenerator, permanent magnets were individually tested to verify full magnetization up to their remanence flux density. Note that the only actuation provided to the device is pressurized gas flow that will be replaced by combusted gas when integrated with a future microcombustion engine. Due to the structurally robust bearing mechanics, no further external magnetic, mechanical, or pneumatic actuation is needed to support the rotor.

B. Stator Phase Electrical Characterization

The dc resistance of the fabricated phase was measured to be 220 Ω. More than 99% of this resistance comes from the sputtered backside connections having three orders of magnitude lower thickness compared to the electroplated parts of the coils embedded in silicon. The ac phase impedance was measured by applying sinusoidal voltages at varying frequencies while
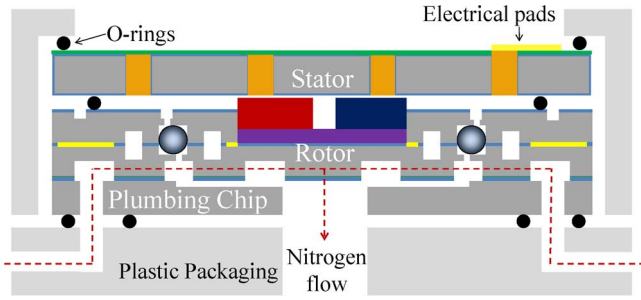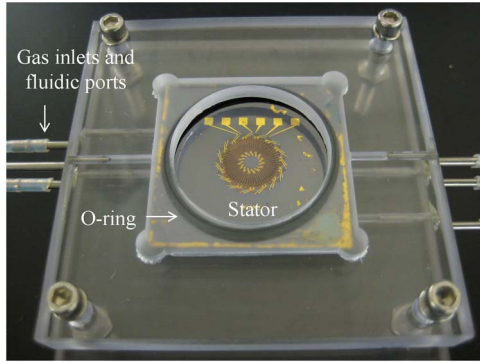
B. Stator

A p-type 400-μm-thick silicon wafer (mold wafer) with low resistivity (1–20 $\Omega \cdot$ cm) was through etched with the coil pattern using DRIE with aspect ratios on the order of 20 [see Fig. 7(a)]. The mold wafer was then thermally oxidized to ensure a high-quality electrical insulation between the adjacent holes. Another wafer (seed wafer) with a 0.5-μm-thick copper seed layer sandwiched in between two 1.5-μm-thick photoresist layers was brought into contact with the mold wafer. Next, the top photoresist layer was exposed through the etched coil pattern and developed, exposing the copper only at the bottom of the through holes [see Fig. 7(b)]. The coil pattern was electroplated with copper [20], and the seed wafer was separated from the mold wafer in an acetone bath [see Fig. 7(c)]. KMPR1050 lithography with a film thickness of 20 μm was then applied on the backside of the mold wafer to passivate the surface and define via openings [see Fig. 7(d)] varying in diameter from 23 to 100 μm. The final connections were made by sputtering and wet etching a 0.2-μm-thick Au film on the KMPR1050 surface [see Fig. 7(e)]. During wet etching, the top side of the stator was protected by a photoresist layer that was later etched away.

A ten-pole three-turns-per-pole device was successfully fabricated with one operational phase. The process yield was low mainly due to the topography of the stator backside after electroplating, making the mask alignment and layer patterning challenging. In addition, the eight-pole four-turns-per-pole and 12-pole three-turns-per-pole designs suffered from disconnections in the inner line vias due to tighter fabrication tolerances.

Fig. 9.   Schematic of the testing setup.

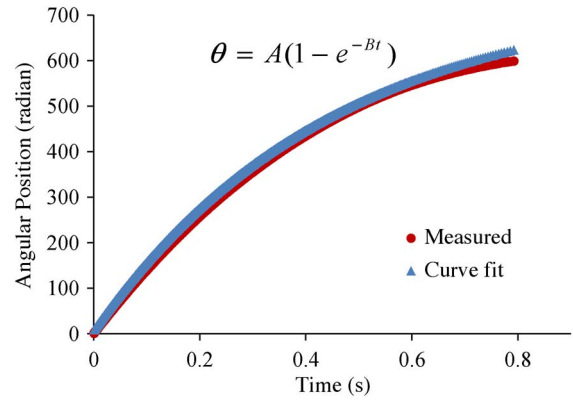Fig. 10.   Photograph of the packaged device.

Fig. 11.   Angular position versus time graph showing the spin down of the rotor from 16 krpm.

Hence, the friction torque becomes $\tau(t) = I \times (d^2\theta/dt^2)$, where $\theta(0)$ and $\theta(0.8)$ correspond to the torque values of 33 μN · m at 16 krpm and 5.5 μN · m at ∼0 krpm, the beginning and the end of spin down, respectively. In comparison to the demonstrations of microball bearings in [15]–[18], the resulting friction torques are higher due to the 44% higher surface area, 20% more microballs in the raceway, and fourfold increase in the total mass.

Once the friction torque is determined, the rotational power dissipated by friction can be calculated by $P = \tau \times (d\theta/dt)$ which yields 50 mW at 16 krpm. The applied pressure and flow values right before the spin down were measured to be 0.75 psi and 9.5 slm, yielding an input fluidic power of 0.82 W. Taking the ratio of these two power values results in a turbine efficiency of 6% at 16 krpm.

simultaneously performing the measurement using a potentiostat. A constant resistance of 220 Ω was observed up to 10 kHz that corresponds to rotational speeds beyond 100 krpm, demonstrating the negligible contributions of the inductances and capacitances to the total impedance in the coils.

C. Microturbine Characterization

The mechanical characterization of the rotor was performed through spin-down testing to measure the friction torque and mechanical loss in the system. In this test, the turbine rotor with integrated permanent magnets was initially spun at 16 krpm with pressurized nitrogen. Next, the flow was stopped, and the rotor decelerated under the effect of friction. The air drag and fluidic losses are assumed to be negligible during spin down due to low Reynold's numbers and device geometry [17]; hence, the deceleration is considered to be due to bearing friction. While the rotor slowed down, angular position versus time data were obtained and recorded using the optical probe and the LabVIEW program. Fig. 11 shows the deceleration of a ten-pole rotor from 16 krpm as a result of the spin-down test.

The previously developed friction model reported in [17] was used to calculate the deceleration of the rotor. In this model, $\theta = A(1 - e^{-Bt})$, where θ is the angular position in radians, A and B are device-dependent constants, and t is the time. A curve was fit to the measured data using this model with an R^2 value of 0.99, yielding A and B to be 740 radians and 2.25 s^{-1}, respectively. The time-dependent deceleration was then calculated by taking the second derivative of this function with respect to time. Assuming that the rotor is a uniform disk, the moment of inertia can be approximated by $I = mr^2/2$, where m is the rotor mass of 0.5 g and r is the 6-mm radius.

D. Microturbogenerator Performance

After testing the stator and rotor separately, these components were combined together for the characterization of the microturbogenerator performance. Initially, open-circuit voltages were measured and recorded at varying rotor speeds up to 23 krpm. The voltage waveforms at selected speeds are plotted in Fig. 12 that demonstrates the increasing frequency and amplitude at increasing speeds. Fig. 13 plots the variation of voltage amplitude with respect to speed, showing an expected linear relationship as dictated by (5). The compliant O-ring between the rotor and the stator yields an air gap in the range of 200–700 μm depending on how tight the plastic manifolds were screwed together on the package. Magnetic field simulations carried out on COMSOL showed average magnetic flux densities of 0.28 and 0.109 T, corresponding to 200- and 700-μm air gaps, respectively. When these values were plugged in (5), theoretical maximum and minimum voltage–speed relationships were obtained and plotted in Fig. 13, showing that the experimental data are in full agreement with the expected theoretical voltage range.

To extract the maximum output power, the matched load condition is created where the impedance of the electrical load is equal to the phase impedance. Accordingly, a 220-Ω resistive load was connected to the terminals of the stator phase. The ac power delivered to the load was calculated by
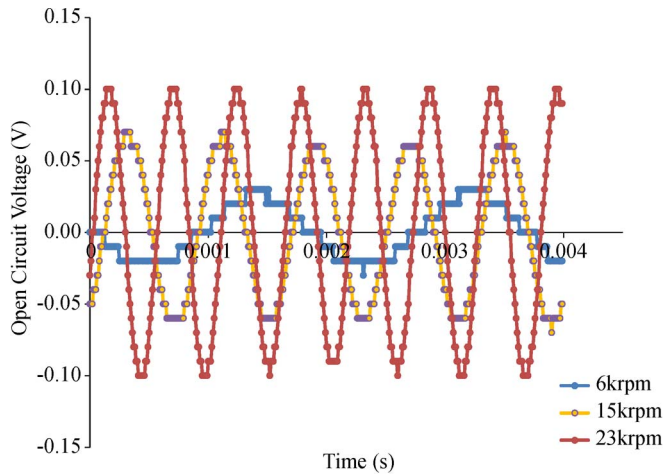
Fig. 12. Induced open-circuit voltages at selected speeds, demonstrating increasing amplitude and frequency at increasing speeds.
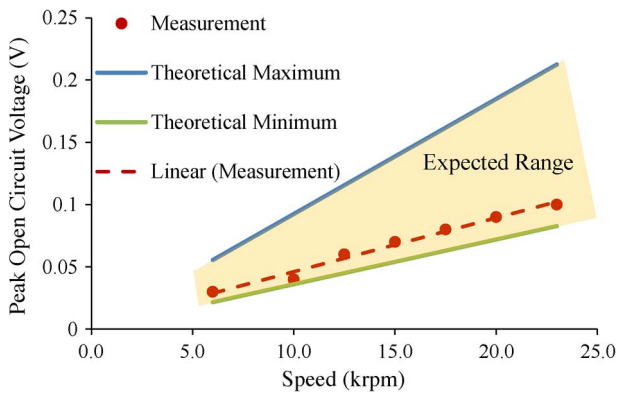

Fig. 13. Open-circuit voltage amplitude as a function of speed and the theoretical voltage–speed range, showing full agreement between the theoretical and experimental results.
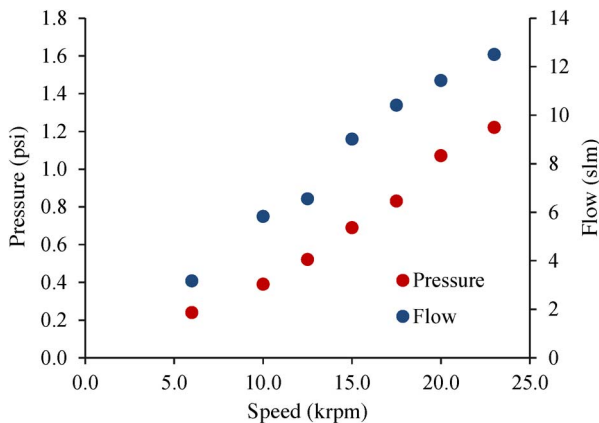

Fig. 14. Applied pressure and flow rate with respect to rotor speed during operation.

the formula $P_{out} = V_{rms}^2/R_{load}$, where V_{rms} is the rms value of the induced voltage over the load resistor R_{load} while the microturbogenerator was being operated at a set speed. Fig. 14 shows the applied pressure and flow rate with respect to speed during operation, while the resulting input and output powers are plotted in Fig. 15, showing expected parabolic behaviors. The maximum delivered power was calculated to be 5.6 μW
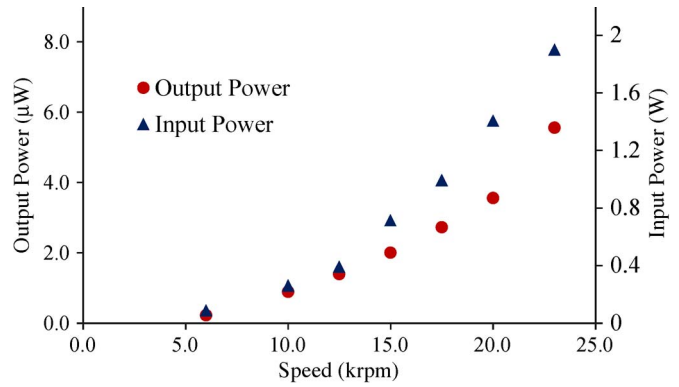

Fig. 15. Input and output powers with respect to rotor speed.
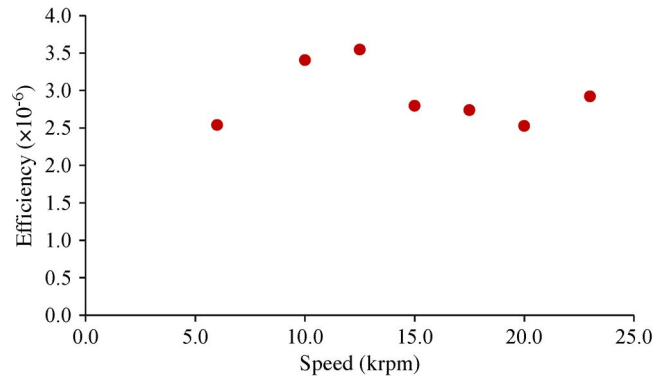

Fig. 16. Calculated fluidic-to-electrical efficiency with respect to rotor speed.

at 23 krpm. Taking the ratio of input and output powers, the efficiency versus speed data were obtained and plotted in Fig. 16 with efficiency values on the order of 3×10^{-6}. Given the dimensions of the device, the active volume is calculated to be 0.17 cm^3 that yields a power density of 33 μW/cm^3. The voltage and power values of the device prohibited the use of diodes and transformers for ac/dc conversion and therefore limited the generation to ac power rather than dc. Higher speeds could not be achieved due to the failure of the rotor eutectic bond beyond 23 krpm. As discussed in the next section, this shows that the limitation in demonstrating higher speeds was not the mechanical stability of the microball bearings but rather microfabrication issues, which can be resolved upon process modifications.

V. DISCUSSION

Test results proved the first successful demonstration of the microturbogenerator with its unique rotor, bearings, and stator components. Good agreement between the theoretical and experimental results showed the accuracy of the electromagnetics analysis and modeling. A direct application of this technology is the development of a small-scale hydrocarbon-based power source, where gas exhaust from a microcombustion engine will be converted to electricity through this device. In this respect, the robustness of the bearings providing a simple operation offers great advantages in the following: 1) the integration of this device with a microcombustion engine and 2) operation in out-of-laboratory environments.

Several design aspects can be further improved as a number of design tradeoffs were made in demonstrating the first functional microturbogenerator. First, the 0.2-μm-thick coil connections sputtered and patterned on the backside of the stator contribute to more than 99% of the total resistance. Electroplating this layer in a polymer mold can increase the thickness to > 100 μm that would result in < 0.1 Ω phase resistance and three orders of magnitude higher power suggested by (6). This will also eliminate the disconnections in the vias and will lead to the successful fabrication of all three phases in different stator designs. In addition, the air gap between the rotor and stator was defined by a compliant O-ring yielding distances on the order of several hundreds of micrometers. The definition of the air gap by four separate microballs placed in etched cavities at the corners of the rotor and stator can provide < 50 μm gaps and < 5 μm alignment tolerance, both increasing the magnetic flux within the stator. Third, the bearing design can be enhanced in terms of the geometry and ball size to allow for higher normal loads. In this respect, an improved bearing geometry with a circular raceway profile is currently under development to accommodate higher loads and higher speeds. This will enable the use of another FeCoV back iron beneath the stator coils to further increase the magnetic flux density and achieve higher output power levels as indicated by (5) and (6).

Finally, an additional factor preventing higher power outputs was the maximum rotor speed in the range of 23 krpm. This speed limit was not defined by the mechanical stability of the microball bearings but rather by the bond strength between the top and bottom rotor wafers. The applied gas flow results in a net torque to spin the rotor, which is also exerted on the bond interface through the turbine blades. Higher flow rates to go beyond 23 krpm are believed to induce enough torque to break the bond between the two rotor wafers. Enlarging the bond area or altering the bonding technique from eutectic to direct silicon-to-silicon bonding is envisioned to allow for higher rotational speeds up to the stability limit of microball bearings. Considering the previously achieved 87 krpm in silicon microturbines [16], an enhanced bonding scheme and the aforementioned circular bearing raceway design is believed to enable rotational speeds beyond 100 krpm.

As a direct result of these design tradeoffs, the measured voltage, power, and power density of the microturbogenerator are lower compared to those of previously demonstrated devices reported in [1]–[11]. First-order calculations using (4)–(6) show that improving the design in the directions explained earlier will lead to four orders of magnitude higher output power in future implementations.

VI. Conclusion

The development of an integrated permanent-magnet microturbogenerator supported on encapsulated microball bearings is presented. The device is composed of a microturbine rotor with thick magnetic materials, integrated microball bearings providing a simple actuation scheme and robust mechanics, and wafer-thick stator coils. The rotor and stator components were optimized through theoretical analysis and finite-element simulations for maximum flux linkage and minimum coil resistance.

A ten-pole three-turns-per-pole microturbogenerator was fabricated and characterized. Stator phase impedance was measured to be a resistive 220 Ω up to 10 kHz. The spin-down testing of the microturbine showed a 33-μN $\cdot$ m friction torque and a 50-mW mechanical power dissipation in the bearings at 16 krpm, corresponding to 6% turbine efficiency. The maximum per-phase ac open-circuit voltage and power were measured to be 0.1 V and 5.6 μW, respectively, at a rotational speed of 23 krpm. Test results are discussed, and possible improvements in device design and fabrication are suggested for higher performance in future implementations. The technology presented in this paper will lead to the development of next-generation integrated microturbogenerators offering high power, simple actuation, and robust mechanics with no need for external actuation apparatus. This will be instrumental in the future integration of this type of generators with microcombustion engines to generate power in out-of-laboratory environments.

References

[1] O. Cugat, J. Delamare, and G. Reyne, "Magnetic micro-actuators and systems (MAGMAS)," *IEEE Trans. Magn.*, vol. 39, no. 6, pp. 3607–3612, Nov. 2003.

[2] D. P. Arnold, "Review of microscale magnetic power generation," *IEEE Trans. Magn.*, vol. 43, no. 11, pp. 3940–3951, Nov. 2007.

[3] A. S. Holmes, G. Hong, and K. R. Pullen, "Axial-flux permanent magnet machines for micropower generation," *J. Microelectromech. Syst.*, vol. 14, no. 1, pp. 54–62, Feb. 2005.

[4] C. T. Pan and T. T. Wu, "Development of a rotary electromagnetic microgenerator," *J. Micromech. Microeng.*, vol. 17, no. 1, pp. 120–128, Jan. 2007.

[5] C. T. Pan and Y. J. Chen, "Application of low temperature co-fire ceramics on in-plane micro-generator," *Sens. Actuators A, Phys.*, vol. 144, no. 1, pp. 144–153, May 2008.

[6] H. Raisigel, O. Cugat, and J. Delamare, "Permanent magnet planar microgenerators," *Sens. Actuators A, Phys.*, vol. 130/131, pp. 438–444, Aug. 2006.

[7] D. P. Arnold, S. Das, J.-W. Park, I. Zana, J. H. Lang, and M. G. Allen, "Microfabricated high-speed axial-flux multiwatt permanent-magnet generators—Part II: Design, fabrication, and testing," *J. Microelectromech. Syst.*, vol. 15, no. 5, pp. 1351–1363, Oct. 2006.

[8] D. P. Arnold, F. Herrault, I. Zana, P. Galle, J.-W. Park, S. Das, J. H. Lang, and M. G. Allen, "Design optimization of an 8 W, microscale, axial-flux, permanent magnet generator," *J. Micromech. Microeng.*, vol. 16, no. 9, pp. S290–S296, Sep. 2006.

[9] B. C. Yen, F. Herrault, K. J. Hillman, M. G. Allen, F. F. Ehrich, S. Jacobson, C.-H. Ji, J. H. Lang, H. Li, Z. S. Spakovszky, and D. R. Veazie, "Characterization of a fully-integrated permanent-magnet turbine generator," in *Proc. 8th Int. Workshop Micro Nanotechnol. Power Gen. Energy Convers. Appl. Power MEMS*, Sendai, Japan, Nov. 9–12, 2008, pp. 121–124.

[10] F. Herrault, C.-H. Ji, and M. G. Allen, "Ultraminiaturized, high-speed, permanent magnet generators for milliwatt-level power generation," *J. Microelectromech. Syst.*, vol. 17, no. 6, pp. 1376–1387, Dec. 2008.

[11] F. Herrault, B. C. Yen, C. H. Ji, Z. S. Spakovszky, J. H. Lang, and M. G. Allen, "Fabrication and performance of silicon-embedded permanent-magnet microgenerators," *J. Microelectromech. Syst.*, vol. 19, no. 1, pp. 4–13, Feb. 2010.

[12] N. Ghalichechian, A. Modafe, J. H. Lang, and R. Ghodssi, "Dynamic characterization of a linear electrostatic micromotor supported on microball bearings," *Sens. Actuators A, Phys.*, vol. 136, no. 2, pp. 416–503, May 2007.

[13] M. I. Beyaz, M. McCarthy, N. Ghalichechian, and R. Ghodssi, "Closed-loop control of a long-range micropositioner using integrated photodiode sensors," *Sens. Actuators A, Phys.*, vol. 151, no. 2, pp. 187–194, Apr. 2009.

[14] N. Ghalichechian, A. Modafe, M. Beyaz, and R. Ghodssi, "Design, fabrication, and characterization of a rotary micromotor supported on microball bearings," *J. Microelectromech. Syst.*, vol. 17, no. 3, pp. 632–642, Jun. 2008.

[15] C. M. Waits, B. Geil, and R. Ghodssi, "Encapsulated ball bearings for rotary micro machines," *J. Micromech. Microeng.*, vol. 17, no. 9, pp. S224–S229, Aug. 2007.

[16] C. M. Waits, M. McCarthy, and R. Ghodssi, "A microfabricated spiral-groove turbopump supported on microball bearings," *J. Microelectromech. Syst.*, vol. 19, no. 1, pp. 99–109, Feb. 2010.

[17] M. McCarthy, C. M. Waits, and R. Ghodssi, "Dynamic friction and wear in a planar-contact encapsulated microball bearing using an integrated microturbine," *J. Microelectromech. Syst.*, vol. 18, no. 2, pp. 263–273, Apr. 2009.

[18] M. McCarthy, C. M. Waits, M. I. Beyaz, and R. Ghodssi, "A rotary microactuator supported on encapsulated microball bearings using an electro-pneumatic thrust balance," *J. Micromech. Microeng.*, vol. 19, no. 9, pp. 094007-1–094007-7, Aug. 2009.

[19] M. Beyaz, B. Hanrahan, and R. Ghodssi, "A microfabricated rotor supported on microball bearings with integrated permanent magnets," in *Proc. 10th Int. Workshop Micro Nanotechnol. Power Gen. Energy Convers. Appl. Power MEMS*, Leuven, Belgium, Nov. 30–Dec. 3, 2010, pp. 167–171.

[20] M. I. Beyaz, M. McCarthy, and R. Ghodssi, "Fabrication of high-aspect ratio metal structures with planar surfaces for power MEMS devices," in *Proc. 9th Int. Workshop Micro Nanotechnol. Power Gen. Energy Convers. Appl. Power MEMS*, Washington, DC, USA, Dec. 1–4, 2009, pp. 586–588.

[21] M. I. Beyaz, B. Hanrahan, J. Feldman, and R. Ghodssi, "An integrated electromagnetic micro-turbo-generator supported on encapsulated microball bearings," in *Proc. 25th IEEE Int. Conf. MEMS*, Paris, France, Jan. 29–Feb. 2, 2012, pp. 1209–1212.

[22] S. Das, D. P. Arnold, I. Zana, J.-W. Park, M. G. Allen, and J. H. Lang, "Microfabricated multiwatt permanent-magnet generators—Part I: Design and modeling," *J. Microelectromech. Syst.*, vol. 15, no. 5, pp. 1330–1350, Oct. 2006.

Mustafa Ilker Beyaz (S'11–M'11) received the B.S. degree in electrical and electronics engineering from the Middle East Technical University, Ankara, Turkey, in 2005 and the M.S. and Ph.D. degrees in electrical engineering from the University of Maryland (UMD), College Park, MD, USA, in 2008 and 2011, respectively.

He joined the Department of Electrical and Electronics Engineering at Antalya International University, Antalya, Turkey, as an Assistant Professor in 2011, where he leads research activities in the field of microelectromechanical systems (MEMS). His research interests lie primarily in the design and development of microsystems for power conversion and energy harvesting, the development of biological sensors and actuators, and the application of nanostructured materials to MEMS devices.

Dr. Beyaz served on the technical program committee of the IEEE Sensors 2012 conference. He is also serving as a peer reviewer for major MEMS journals. He is the recipient of two doctoral research awards from the Department of Electrical and Computer Engineering and the James Clark School of Engineering at UMD.

Brendan Michael Hanrahan (S'11–M'96) received the B.S. degree in ceramic and materials engineering from Clemson University, Clemson, SC, USA, in 2006 and the M.S. and Ph.D. degrees in materials science and engineering from the University of Maryland, College Park, MD, USA, in 2009 and 2013, respectively.

Since 2009, he has been a Materials Engineer with the U.S. Army Research Laboratory in the Sensors and Electron Devices Directorate Adelphi, MD, USA. His research interests include the tribology of high-performance microelectromechanical systems (MEMS) and the development of MEMS components for compact portable power systems.

Jeremy Feldman received the B.S. degree in electrical engineering from the University of Maryland, College Park, MD, USA, in 2011 with concentrations in microelectronics, nanomaterials, and power systems. His undergraduate research was in high-density thin-film capacitors, optical structured nanomaterials for photovoltaics and sensors, nano-level security markers, and an extensive study of vibration and wear in rotary microelectromechanical systems (MEMS) devices supported on microball bearing technology. He is currently conducting research at the MEMS Sensors and Actuators Laboratory located at the University of Maryland and working toward the M.S. degree in systems engineering, with a focus in optical methods for biosensing, and biofeedback systems.

Reza Ghodssi (S'92–M'96) received the B.Sc., M.Sc., and Ph.D. degrees from the Department of Electrical Engineering, University of Wisconsin, Madison, WI, USA, in 1990, 1992, and 1996, respectively.

He is currently the Herbert Rabin Distinguished Chair in Engineering, the Director of the Institute for Systems Research, and the Director of the MEMS Sensors and Actuators Laboratory, Department of Electrical and Computer Engineering, University of Maryland (UMD), College Park, MD, USA. He is also currently with the Fischell Department of Bioengineering, the Maryland NanoCenter, the University of Maryland Energy Research Center, and the Materials Science and Engineering Department, UMD. His research interests are in the design and development of microfabrication technologies and their applications to micro-/nanodevices and systems for chemical and biological sensing, small-scale energy conversion, and harvesting. He has over 95 refereed journal publications. He was the Coeditor of the *Handbook of MEMS Materials and Processes* (Springer, 2011) and is an Associate Editor for the JOURNAL OF MICROELECTROMECHANICAL SYSTEM and *Biomedical Microdevices*.

Dr. Ghodssi is a member of the American Vacuum Society, the Materials Research Society, the American Society for Engineering Education, and the American Association for the Advancement of Science. He was the Chair of the "NSF Workshop on Micro Nano Bio Systems" in 2012. He was also the Chair of the 9th International Workshop on Micro and Nanotechnology for Power Generation and Energy Conversion Applications, also known as "PowerMEMS 2009," and the Americas Technical Program Committee Chair of the IEEE Sensors 2010, 2011, and 2012 Conferences. He is the Cofounder of MEMS Alliance in the greater Washington DC, area. He was the recipient of the 2001 UMD George Corcoran Award, a 2002 National Science Foundation CAREER Award, and the 2003 UMD Outstanding Systems Engineering Faculty Award.